UC Davis
UC Davis Previously Published Works

Title

Referenced Kendrick Mass Defect Annotation and Class-Based Filtering of Imaging MS Lipidomics Experiments.

Permalink

https://escholarship.org/uc/item/6rx1n4h2

Journal

Analytical Chemistry, 94(14)

Authors

Richardson, Luke
Neumann, Elizabeth
Caprioli, Richard
et al.

Publication Date

2022-04-12

DOI

10.1021/acs.analchem.1c03715

Peer reviewed

Referenced Kendrick Mass Defect Annotation and Class-Based Filtering of Imaging MS Lipidomics Experiments

Luke T. Richardson,

Department of Chemistry and Biochemistry, Baylor University, Waco, Texas 76706, United States

Elizabeth K. Neumann,

Department of Biochemistry, Vanderbilt University, Nashville, Tennessee 37205, United States; Mass Spectrometry Research Center, Vanderbilt University, Nashville, Tennessee 37235, United States

Richard M. Caprioli,

Department of Biochemistry, Vanderbilt University, Nashville, Tennessee 37205, United States; Mass Spectrometry Research Center and Department of Medicine, Vanderbilt University, Nashville, Tennessee 37235, United States; Department of Chemistry, Vanderbilt University, Nashville, Tennessee 37235, United States; Department of Pharmacology, Vanderbilt University, Nashville, Tennessee 37235, United States

Jeffrey M. Spraggins,

Department of Biochemistry, Vanderbilt University, Nashville, Tennessee 37205, United States; Mass Spectrometry Research Center and Department of Cell and Development Biology, Vanderbilt University, Nashville, Tennessee 37235, United States; Department of Chemistry, Vanderbilt University, Nashville, Tennessee 37235, United States

Touradj Solouki

Department of Chemistry and Biochemistry, Baylor University, Waco, Texas 76706, United States

Abstract

Because of their diverse functionalities in cells, lipids are of primary importance when characterizing molecular profiles of physiological and disease states. Imaging mass spectrometry

Corresponding Author: Touradj Solouki – Department of Chemistry and Biochemistry, Baylor University, Waco, Texas 76706, United States, Touradj_Solouki@baylor.edu.

Author Manuscript Author Manuscript Author Manuscript Author Manuscript

(IMS) provides the spatial distributions of lipid populations in tissues. Referenced Kendrick mass defect (RKMD) analysis is an effective mass spectrometry (MS) data analysis tool for classification and annotation of lipids. Herein, we extend the capabilities of RKMD analysis and demonstrate an integrated method for lipid annotation and chemical structure-based filtering for IMS datasets. Annotation of lipid features with lipid molecular class, radyl carbon chain length, and degree of unsaturation allows image reconstruction and visualization based on each structural characteristic. We show a proof-of-concept application of the method to a computationally generated IMS dataset and validate that the RKMD method is highly specific for lipid components in the presence of confounding background ions. Moreover, we demonstrate an application of the RKMD-based annotation and filtering to matrix-assisted laser desorption/ionization (MALDI) IMS lipidomic data from human kidney tissue analysis.

Graphical Abstract
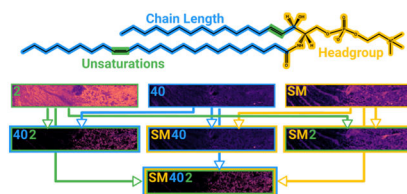
Imaging mass spectrometry (IMS) provides valuable identity, abundance, and spatial distribution information for molecular components of complex biological tissues. A variety of IMS approaches are used to explore molecular profiles of many biological systems and measure small metabolites,[1–4] lipids,[5–8] peptides,[9–11] glycans,[12–14] and proteins.[15–17] Among these molecular classes, lipids are essential for cell signaling, membrane composition, and metabolism[18–20] but are difficult to study by non-MS means such as immunostaining or transcriptomics. Matrix-assisted laser desorption/ionization (MALDI) IMS is a powerful tool to measure lipids at 10 μm spatial resolutions approaching the size of a mammalian cell.[9,21] In MALDI analyses, tissue sections between 5 and 20 μm are thaw-mounted on conductive glass slides and uniformly covered with a chemical matrix that absorbs ultraviolet radiation and promotes desorption and ionization of endogenous molecules, including lipids.[9,22,23] Ion intensities from mass spectra acquired from each pixel are visualized to produce spatially resolved ion images.[24] Because of the abundance and diversity of lipids, resultant IMS spectra can be complex;[7] detected lipids are often isomeric and/or isobaric and cannot be resolved by using high mass resolving power alone. Therefore, often ultrahigh mass resolving power instruments are used for isobar separation[25,26] and other analysis dimensions such as ion mobility separation,[7,27] low energy CID,[28] or chemical modification[29,30] are utilized to assign double-bond position and stereospecifically numbered (*sn*) position isomers. Given the direct biosynthetic relationships within lipid families, methods that can identify lipids, link lipid families, and preserve their spatial distributions in tissues are essential for investigating lipid biochemistry.

Kendrick mass defect (KMD) analysis can deduce families of chemically related compounds, such as lipids, using high-resolution MS data in a variety of different fields of study.[31–33] In KMD analysis, the atomic mass unit reference is changed from ^{12}C to

other groups, such as methylene (or CH_2, often using $^{12}C_1$ and $^1H_2$ isotopes for carbon and hydrogen atoms) or other units that repeat in polymer chain elongation. Thus, the Kendrick mass is the monoisotopic mass-to-charge ratio (m/z) value adjusted to the new reference; the resultant mass deficiency or defect, usually rounded to the nearest integer unit, can be used to discriminate molecular classes that contain varied mass deficiencies. Given that the CH_2-based KM scale eliminates all CH_2 mass defect contributions, molecules such as lipids that differ by aliphatic chain length have the same KMD and those with differing degrees of unsaturation exhibit KMD differences of 0.01335 per unsaturation, which corresponds to the KMD of H_2. De Pauw et al. demonstrated a KMD-based IMS visualization tool that filtered MALDI MS images based on lipid features clustered in KMD space.[32] Although molecular families could be grouped by untargeted clustering algorithms, analyte assignments were provided by exact mass matching, and molecular classes of clusters were inferred. As evidenced in this visualization tool, KMD analysis is well suited to lipidomics; however, the more specialized referenced KMD (RKMD) approach can provide more direct information about lipid molecular families.[34]

Lerno et al. demonstrated that RKMD can be used to determine the class and degrees of unsaturation for lipidomics experiments.[34] In RKMD analysis, the reference KMD of a specified lipid headgroup is subtracted from the analyte KMD, and the difference is divided by 0.0134. Theoretically, if the resulting quotient is equal to the integer value of zero or less, it is indicative of a positive classification for a specified lipid headgroup. Moreover, the absolute value of the RKMD value indicates the degrees of unsaturation. However, mass measurement errors often preclude an error-free case, and thus, RKMD values that predict correct chemical classes might not be an exact integer value. Additionally, the presence of confounding peaks in mass spectra (such as those from heavy isotopologues, MALDI matrix species, solvent clusters, and other molecular classes) presents challenges for conventional RKMD analyses that lack controls to ensure specificity in lipid classification. Lerno et al. employed heuristic constraints that limited false-positive classifications but simultaneously limited the MS analysis to lipids with less than or equal to six degrees of unsaturation. This provides an opportunity for method improvements to expand the coverage of the RKMD analysis to a wider subset of the lipidome.

Herein, we report a method for lipid feature annotation and class-based image filtering for lipidomics IMS data using an RKMD-based approach. We utilized both computationally generated and experimental MALDI MS imaging datasets from human kidney tissues to assign lipid features via RKMD determination of lipid molecular classes, degrees of unsaturation, and numbers of radyl carbons. The latter is a novel extension of RKMD analysis that allows for increased method specificity and precision as well as lipid assignment. We show that class-specific spatial distributions of lipid populations can be used for automated image filtering and visualization of lipid descriptors such as molecular class, unsaturation, and radyl carbons. In previous approaches, spatial analyses depended on targeted identification of lipids by instrumental methods and user input to determine relationships in and between chemically related groups of lipids. In contrast, the presented method provides an integrated means for identification, annotation, and rapid visualization of related lipids in IMS datasets.

EXPERIMENTAL SECTION

Sample Preparation.

Human kidney tissues were collected as part of normal non-neoplastic portions of nephrectomy samples for research purposes by the Cooperative Human Tissue Network at Vanderbilt University Medical Center.[35] Remnant biospecimens were collected in compliance with the Cooperative Human Tissue Network standard protocols and National Cancer Institute's Best Practices for the procurement of the remnant surgical research material. The excised tissue was flash-frozen over an isopentane and dry ice slurry, embedded in carboxymethylcellulose, and stored at negative 80 °C until use. The kidney tissue was cryosectioned to a 10 μm thickness, thaw-mounted onto indium tin-oxide (ITO)-coated glass slides (Delta Technologies, Loveland, CO) for IMS analysis. Tissues were stored at negative 80 °C and returned to ~20 °C within a vacuum desiccator. IMS samples were coated with a 20 mg/mL solution of 1,5-diaminonapthalene (DAN) dissolved in THF using an HTX TM M3 Sprayer (HTX Technologies, LLC, Chapel Hill, NC) yielding a 1.67 mg/cm^2 coating (0.05 mL/h, 5 passes, 40 °C spray nozzle). Tissue samples underwent IMS analysis immediately after matrix deposition.

MALDI TimsTOF IMS.

MALDI IMS was performed on a prototype Bruker timsTOF pro MS system[21] (Bruker Daltonics, Bremen, Germany) in quadrupole-time of flight (qTOF) only analysis mode. The qTOF ion images were collected in positive-ion mode at 10 μm pixel size. The laser beam scan was set to 6 μm^2 and 200 laser (λ = 266 nm) shots per pixel at 10 kHz for laser desorption and 18.6% laser power (30% global attenuator and 62% local laser power). Mass spectrometry data were collected from m/z 50 to 2000 in centroid mode for lipid analysis. Provisional identifications of tissue lipids were produced using a combination of mass accuracy (3 ppm) and LIPIDMAPS[36,37] database searching. Only even chained lipids were considered because mammalian systems do not generally produce odd-chain lipids, except in special circumstances.[38,39]

Computational Generation of IMS Data.

Theoretical isotopic envelopes for lipids, MALDI matrix clusters, and peptide ions were calculated using the pyOpenMS (2.6.0) Python package to provide a proof of concept and to test the specificity and precision of the RKMD-based method. Peptides and MALDI matrix clusters were used to test the specificity of the method for lipids in the presence of confounding species. Lipid chemical formulas were acquired from the LIPIDMAPS structure database (LMSD). Each lipid isotopic envelope was generated from the chemical formula of the protonated, singly charged molecular ion and data for three isotopologues were calculated and used in subsequent analyses. The isotopic envelopes for MALDI matrix (M) cluster ions were calculated for monomeric $[M + H]^+$ and proton bound dimeric $[2M + H]^+$, trimeric $[3M + H]^+$, and tetrameric $[4M + H]^+$ ion clusters of 2,5-dihydroxybenzoic acid (DHB), α-cyano-4-hydroxycinnamic acid (CHCA), and DAN. In addition, isotopic envelopes for fragment ions resulting from common neutral losses (H_2O and CO_2 from DHB and CHCA and NH_3 from DAN) as well as sodium and potassium adducts were included as potential confounders; sodiated and potassiated cluster ions were generated

according to the rules described by Keller et al.[40] DHB, CHCA, and DAN are three common choices for MALDI matrix in positive-ion mode lipidomics MALDI IMS experiments and provide good ionization for a variety of lipid classes.[41] Peptide chemical formulas were converted from randomly generated peptide sequences with chain lengths between 1 and 25 amino acids. Each peptide isotopic envelope was synthetically generated from singly charged and protonated species and included seven isotopologue peaks. Continuum mass spectra (i.e., with multiple sampled points over each peak) were generated by calculating the gaussian distribution of each isotopologue along an m/z axis from m/z 100 to 1500. The m/z centroid and relative isotopic abundance values were input for the mean and amplitude in the Gaussian function. Given that resolving power remains relatively constant across the mass range in TOF instrumentation,[42] the Gaussian sigma parameter was held constant across the m/z range and produced peaks with mass resolving powers ($m/\Delta m_{50\%}$) ranging from ~55 000 to 65 000.

To test the specificity and precision of the RKMD annotation method, five MS datasets consisting of theoretical centroid m/z values were generated for protonated, sodiated, and potassiated lipids, MALDI matrix clusters, and peptides. Lipid components included protonated, sodiated, and potassiated ions of 500 lipids, including 62 phosphatidylcho-line (PC), 60 phosphatidylethanolamine (PE), 61 phosphatidic acid (PA), 62 phosphatidylglycerol (PG), 59 diacylglycerol (DG), 22 sphingomyelin (SM), 32 triacylglycerol (TG), 40 ether-linked (O/P-) PC, 35 O/P-PE, 33 O/P-PA, and 34 O/PPG. Lipids were chosen pseudo-randomly from LMSD and had even chains between 28 and 50 radyl carbons and 0 and 9 unsaturations from 11 common lipid classes. The peptide ion spectrum was generated from 1000 unique peptide sequences, resulting in 7000 total peaks. The MALDI matrix ion spectrum was generated from 1305 matrix cluster species, resulting in 3915 total peaks.

The computationally generated IMS dataset was based on a .PNG image depicting the letters "BU & VU", and each letter had a unique set of RGB color values. The RGB color values in the image were associated with collections of lipid ion isotopic envelopes related by lipid molecular class, degree of unsaturation, or number of radyl carbons. At each coordinate in an equivalently sized two-dimensional array, a spectrum extending in the 3rd dimension was generated using the lipid species of the appropriate class. The "BU" coordinates included spectra containing MS isotopic envelopes from 86 O/P-PG lipids with 0 to 6 double bonds and 28 to 40 radyl carbons (even radyl carbon chains only). However, "&" coordinates included spectra containing MS peaks from 216 MS isotopic envelopes from lipids with 4 double bonds in the PC, PA, PG, and DG classes and with 28 to 40 radyl carbons (even radyl carbon chains only). Finally, "VU" coordinates included spectra that contained MS isotopic envelopes from 257 lipids with 34 radyl carbons in the PC, PA, PG, and DG classes and with 0 to 6 double bonds.

MALDI IMS Data Preprocessing.

Bruker MALDI IMS data was converted to the imzML file format prior to peak picking and then to a native Python dictionary structure with custom Python (3.8.5, CPython, Python Foundation) scripts (preprocessing, annotation, and filtering Python scripts are

publicly available at https://github.com/luketrichardson/RKMD-MS-Image-Annotation-and-Filtering). Data for un-sampled coordinates between the maximum x and y image coordinate were filled with an empty spectrum to make the data amenable to numpy array operations and matplotlib image visualization in Python. An internal, quadratic recalibration of the summed spectrum was performed using six common lipid features $[PC(32:0) + H]^+$, $[PC(34:1) + H]^+$, $[PC(34:1) + Na]^+$, $[PC(36:1) + H]^+$, $[PC(34:1) + K]^+$, and $[PC(36:1) + Na]^+$, resulting in <3 ppm error. Each peak within each MALDI IMS spectrum was aligned to the recalibrated summed spectrum. Recalibration and alignment are important to mitigate the effects of m/z drift and noise on mass measurement error. The effect of the signal-to-noise ratio (SNR) on mass measurement error was evaluated for the RKMD annotation workflow, and RKMD feature annotation was found to be generally robust down to the signal detection limit (Figure S1).

RKMD-Based Lipid Annotation.

Overall, we annotate lipids with their sum compositions using an RKMD-based workflow that uses mass spectrometry data to assign lipid sum compositions with headgroup, radyl carbon chain length, and unsaturation information. A representative schematic of the lipid annotation using this RKMD approach is included in the Supporting Information (Scheme S1). First, the synthetically generated or experimentally acquired IMS dataset was input to the annotation workflow in a Python dictionary structure. On a per pixel basis, the centroid spectrum was read and aligned to the recalibrated summed spectrum. A recalibrated summed spectrum was used to bin m/z values and enhance mass measurement accuracy by recalibrating the average m/z values in all acquired mass spectra. Once the mass spectrum was realigned, RKMD analysis was performed for each peak in the spectrum for the molecular class headgroup and adduct RKMD. Twenty different lipid headgroup elemental compositions (Table S1) and various commonly observed adducts (Table S2) were used to calculate the reference KMD for each lipid class and its commonly observed adducts. Specifically, the reference KMD of the adducted headgroup of each lipid class was calculated and subtracted from the experimentally acquired KMD value. The resulting difference was then divided by 0.0134 (CH_2-based Kendrick mass defect of carbon) to produce the RKMD value.[34]

For each calculated RKMD value, its distance from the closest integer value (δ) was determined. The features that produced an RKMD δ within a user-defined window ($\delta = 0.35$ in this work) for RKMD values between 0 and −9 (corresponding to 0 and 9 unsaturations, respectively) were considered potential positive annotations for the class-of-interest; features that did not meet these criteria were excluded from further processing. The corresponding headgroup and unsaturation information were used to calculate the number of radyl carbons for each potential positive classification. Analogous to using δ acceptance windows, the distance from the calculated integer values indicating numbers of radyl carbons (ε) was used to exclude erroneous classifications. Peaks with radyl carbon ε values greater than 0.001 were excluded from downstream processing steps as true positive identifications were found to have radyl carbon ε 0.001. Positive integer results were considered unacceptable results, not in agreement with physical reality.[34] For each potential annotation, m/z, lipid class, adduct, number of radyl carbons, degree of unsaturation, radyl carbon ε, RKMD δ, even

number radyl carbons (true or false), and peak intensity were stored in a Python dictionary. This process was repeated for every molecular class headgroup and an adduct of interest.

Image Filtering and Heuristic Constraints.

Lipid distributions were then visualized based on lipid classes defined by similarities in the lipid headgroup, degrees of unsaturation, and the number of radyl carbons. As an example, a filter for the O/P-PE class is applied for RKMD assignments of m/z 790.5151, which include [PC(O/P-35:5) + K]$^+$,[PE(O/P-38:5) + K]$^+$, [LPC(35:5) + K]$^+$, and [LPE(38:5) +K]$^+$ (Scheme S2). First, assignments were rank-ordered by ascending RKMD δ values for each peak at each pixel. To limit false-positive identifications, several heuristic constraints were applied. Lower and upper limits were placed on the numbers of radyl carbons and degrees of unsaturation that were accepted for each lipid molecular class (Table S3). Limits were based on commonly observed fatty acids[43] and radyl carbon chain lengths for each lipid molecular class in MALDI IMS tissue analyses.[6,44] Molecular class-specific degree of unsaturation limits were necessary to curtail false-positive identifications in which unrealistically high degrees of unsaturation were calculated.[34] Additionally, odd numbered radyl carbon chains were excluded given that odd-chain fatty acids are uncommon in human tissues.[38,39] After excluding potential annotations by heuristic constraints, the top-ranked assignment was compared to the filter criterion, and the RKMD δ was compared to an m/z value-dependent error limit. If the filter criterion matched the assignment and the RKMD δ was below the error limit, the feature intensity was added to the pixel intensity of the filtered image. The RKMD δ error limit was calculated by eq 1 where δ is the error limit expressed in terms of RKMD δ, p is the error limit expressed in terms of ppm error, m is the m/z value of the feature, and 13415 is a constant that

$$\delta = \frac{p}{13415m^{-1}} \tag{1}$$

relates RKMD δ to ppm error to approximate a 2.5 ppm error threshold. The relationship between RKMD δ and ppm error is inversely related (Figure S2). Given that RKMD δ is necessarily 0.5 for any feature, the maximum error limit that may be utilized is dependent on eq 1 as a function of m/z. Although annotations were constrained to highly accurate annotations in this demonstration (<2.5 ppm error), there is no mass accuracy requirement (besides that determined by eq 1 at $\delta = 0.5$) given that annotations are rank-ordered among other putative identifications as in conventional exact mass database searching workflows. In general, the RKMD workflow is broadly compatible with medium to ultrahigh mass resolving power MS instruments that routinely achieve <5 ppm mass measurement error following internal calibration.

RESULTS AND DISCUSSION

RKMD-Based Annotation and Filtering of Computationally Generated IMS Data.

Data processing and analysis methods in IMS have advanced significantly in recent years to accelerate the analysis of large data volumes. Data analysis of IMS is often conducted manually by selective visualization of m/z values or by unsupervised data reduction (e.g., principal component analysis (PCA)[45]) and/or segmentation approaches[46] that group

pixels/spectra by similarity.[47,48] However, manual analysis can be time consuming, and unsupervised analyses do not describe the relationships between pixel groups or may produce uninterpretable results.[46] Biologically relevant conclusions are therefore dependent on the accurate class-based annotation of molecular species in biomarker discovery workflows. Chemical class annotation is useful to analyze global trends in data, and one attractive option for lipid class annotation is the RKMD method.[34] However, in conventional RKMD, there is a potential for false-positive classifications from confounding ions because the only criterion for chemical classification is an acceptance window for RKMD values determined by mass measurement error. To address this drawback and adapt RKMD for imaging applications, we implemented an additional data curation criterion to reduce potential incorrect results and expand the RKMD approach's analytical capabilities from classification to full sum composition lipid annotation. The advantage of this type of lipid annotation and data analysis is that multiple tissue images, based on the user-defined lipid classes, can be generated to study potential correlations and relationships between different lipids and lipid classes.

In this approach, we increase the specificity and precision of RKMD-based annotation via exclusion of true-negative peaks based on the distance from calculated radyl carbon integer values. The specificity and precision of the RKMD-based annotation method are demonstrated in application to a computationally generated complex dataset containing lipids and potentially confounding species, including MALDI matrix cluster and peptide ions (Figure 1). Confounding species were included to evaluate the performance of the approach for their effective exclusion. MALDI matrix cluster ions are often observed as background ions in MALDI experiments.[49] Likewise, peptides are potential confounders in tissue IMS lipidomics; although they are not often detected concurrently with lipids in tissue IMS experiments except in single-cell[10] and small-metabolite[1] analyses.

The computationally generated ions were subjected to RKMD analysis and results are displayed as plots of RKMD as a function of Kendrick nominal mass (KNM) (Figure 1A–F). Each row of plots was subjected to a different level of data curation. In this work, [PG + H]$^+$ was chosen as a reference lipid headgroup as it exhibited the lowest specificity of all classes included in the dataset. In Figure 1, MALDI matrix cluster ions are displayed in green, peptide ions are displayed in pink, and lipids are shown in three different colors blue (protonated), purple (sodiated), and orange (potassiated). Plots labeled "All Peaks" (Figure 1A–C) contain the entire dataset, whereas plots labeled "Positive ID Region" (Figure 1D–F) show the relevant regions for RKMD classifications. Prior to any data curation, 1112 peptide, 498 MALDI matrix cluster, and 2596 true-negative lipid MS datapoints were observed in the zoomed positive ID region (Figure 1D).

For comparison, lipid, matrix cluster, and peptide data were first curated by RKMD δ exclusion only with a window of 0.1 or ~1.9 ppm mass error (Figure 1B,E). This case reflects a conventional application of RKMD wherein retained datapoints would indicate positively classified species for the specified headgroup. By imposing the RKMD δ exclusion value of 0.1, 20.1% (1410) of the 7000 peptide datapoints in the total space were retained (Figure 1B), and 20.6% (229) of the 1112 peptide datapoints in the positive ID region were retained (pink, Figure 1E). Similarly, 20.4% (799) of the 3915 MALDI

matrix cluster datapoints in the total space were retained (Figure 1B), and 19.5% (97) of the 498 matrix cluster datapoints in the positive ID region were retained (green, Figure 1E). Of the retained lipid datapoints, 55 corresponded to $[PG + H]^+$ monoisotopic peaks, and 358 corresponded to heavy isotopologues and/or peaks from other lipid molecular classes. In the total RKMD space (Figure 1B), the specificity for correct exclusion of non-$[PG + H]^+$ monoisotopologues was 83.3% (ratio of true-negative indications to all negatives), and the precision (ratio of true-positive indications to all positive indications) imparted by RKMD δ exclusion was 2.1%. In the positive ID region, these numbers for the specificity and precision improved to 89.9 and 11.4%, respectively (Figure 1E). Although a significant portion of the confounders was excluded by utilizing an RKMD δ window (Figure 1E), this conventional approach lacks the desired level of specificity and precision for confident lipid annotation.

To demonstrate the enhancement provided in the presented RKMD-based annotation workflow, the number of radyl carbons were calculated for each feature assuming a $[PG + H]^+$ headgroup, and data were curated by a radyl carbon ε exclusion window of 0.001 in addition to an RKMD δ exclusion window of 0.1 (Figure 1C,F). Application of radyl carbon ε exclusion with a window of 0.001 decreased the number of retained peptide datapoints from 1410 (peptides retained by RKMD δ exclusion only) to only 79 (1.1% of 7000 total) and matrix cluster peaks from 773 to 64 (1.6% of 3915 total) in the total space (Figure 1C). In the RKMD positive ID region (Figure 1F), radyl carbon ε exclusion decreased retained peptide datapoints from 229 to 26 (2.3% of 1112) and MALDI matrix cluster datapoints from 97 to 8 (1.6% of 498). All potential lipid false-positives were eliminated, leaving only the 55 peaks corresponding to the $^{12}C_{all}$ isotopologues of $[PG + H]^+$ components (Figure 1C,F). This corresponds to a true-positive rate of 100% for positive identification of all $[PG + H]^+$ lipids. In the positive ID region (Figure 1F), specificity was increased to 98.8% (from 89.9% for RKMD δ exclusion only) and precision to 78.6% (from 11.4% with only RKMD δ). Successful exclusion of most matrix clusters and peptide ions (98.4 and 97.7%, respectively) suggests that the method is robust in excluding nonlipid components (Figure 1).

Moreover, the observed enhancement in this new approach enabled assignment of highly unsaturated lipids with greater confidence, relative to the conventional RKMD δ windowing exclusion approach via elimination of false-positive lipid assignments from both heavy isotopologue peaks and monoisotopic peaks of other classes. For instance, when solving for $[PC + H]^+$ RKMD values, $[PA(34:1) + K]^+$, $[PA(38:4) + K]^+$, and $[PA(36:6) + K]^+$ monoisotopic peaks produce low RKMD δ values at integers −7, −10, and −12, respectively (purple diamonds, node III, Scheme S1), and therefore reduce confidence in highly unsaturated PC assignments in conventional RKMD analyses. However, solving for each $[PA+K]^+$ component's radyl carbon chain length (assuming a $[PC + H]^+$ headgroup) produces large radyl carbon ε values exceeding the threshold of 0.001 used in this work (purple diamonds, Scheme S1, node IV), restoring confidence to highly unsaturated $[PC + H]^+$ assignments.

As a proof of concept, the RKMD-based annotation and filtering method was applied to a computationally generated IMS dataset comprised of theoretical MS peaks (Figure 2).

The total ion current (TIC) image of the dataset (Figure 2B) displays contributions from 559 protonated lipid MS peaks spatially arranged to display the text "BU & VU". The summed mass spectrum of all included lipid components is displayed on top of the TIC image and is notably complex (Figure 2A). RKMD-based annotation correctly assigned each lipid, and the filtering method reconstructed each select class image using RKMD δ and radyl carbon ε exclusion windows of 0.1 and 0.001, respectively. Specifically, reconstructed images for 86 ether-linked phosphatidylglycerol lipids at "BU" coordinates (Figure 2C), 216 lipids with four degrees of unsaturation from PC, PA, PG, and DG chemical classes at "&" coordinates (Figure 2D), and 257 lipid features with 34 radyl carbons from PC, PA, PG, and DG chemical classes at "VU" coordinates (Figure 2E) are shown in Figure 2C–E. Each selected image represents a filtering mode that utilizes a different criterion, namely, lipid chemical class (Figure 2C), degrees of unsaturation (Figure 2D), and number of radyl carbons (Figure 2E). The RKMD-based reconstructed images demonstrate that this class-based filtering approach can be used to ascertain the character and localization of related groups of lipids in IMS data (Figure 2). To evaluate the utility of the RKMD-based lipid annotation for tissue image reconstruction, we analyzed MALDI IMS data from human kidney tissues and highlighted the advantages of a class-based approach for spatial tissue characterization.

MALDI IMS of Kidney Tissue Lipids.

The presented workflow was applied to a MALDI tissue imaging analysis of human kidney lipids. Lipids are of primary importance to the healthy functioning of kidney tissues and characterization of renal disease.[50,51] MALDI MS has enabled detailed interrogations into the spatial distribution and composition of different lipids in human kidney tissues that have provided key insights into physiological and disease mechanisms.[52–54] The imaged kidney section (220 000 pixels) contains portions of the medulla and cortex. Subsections of these regions are visible at varying degrees in all class-based images, such as medullary rays, proximal tubules, collecting ducts, blood vessels, and glomeruli (Figure 3). A composite of all saturated lipids and monounsaturated PC lipids is shown in Figure 3 (top and bottom, respectively). To confirm the accuracy of the RKMD-based annotation method, 44 m/z values that resulted in provisional identifications made by a combination of mass accuracy and LIPIDMAPS database searching were submitted to RKMD-based annotation. The RKMD-based method produced equivalent assignments in each case after the application of the heuristic constraints used in the presented image filtering workflow (Table S4).

Observed lipids from MALDI IMS of kidney tissues from several different molecular classes were detected and assigned by the RKMD workflow. At the highest level, resultant images are composites of all assigned lipid components that are grouped by molecular class, unsaturation, and radyl carbon chain length (Figure S3). Although the high-level class composite images may be useful to evaluate broad differences in lipid class distributions in tissues, localization of related lipids can vary significantly with respect to other characteristics, such as localization of a lipid class with varying radyl carbon chain lengths or degrees of unsaturation. Some lipid isomers can even have differing spatial distributions in tissues; however, these differences cannot be visualized without an orthogonal dimension of separation such as ion mobility.[7] However, in the interest of

preserving spatial information, all molecular metadata for each component was retained such that subclass images of more specific groupings of lipids could be easily reconstructed and compared to evaluate localization of lipid classes with finer differences.

For example, lipid distributions corresponding to saturated and monounsaturated PC and PE and mono- and diunsaturated SM components were evaluated (Figure 4). Images of saturated PC (Figure 4A) and PE (Figure 4B) and monounsaturated SM (Figure 4C) components are highly colocalized in the kidney tissue, showing high abundance within the glomeruli, blood vessels, and medullary rays (Figure 3). Previously, SM lipids have been characterized throughout the renal cortex and medulla; moreover, studies have characterized localization of monounsaturated SM to glomeruli in healthy rat subjects[55] and in diabetic mouse subjects in response to a high-fat diet.[52] In contrast, images of monounsaturated PC and PE (Figure 4D,E) both show different spatial distributions compared to saturated PC and PE (Figure 4A,B). Although some low signal may be observed from the glomeruli in the cortex, the signal arises primarily from the proximal tubules. In the medulla, monounsaturated PC and PE (Figure 4D,E) are colocalized to the renal collecting ducts; in the cortex, monounsaturated PC and PE highlight elements of the renal cortical labyrinth and proximal tubules that surround the glomeruli. Concerning the blood vessels, saturated (Figure 4A,B) and unsaturated PC and PE (Figure 4D,E) are negatively correlated. Saturated PC and PE colocalized to structures above the central blood vessel (light blue bracket, Figure 4A), and unsaturated PC and PE have higher abundance in the tissues surrounding the blood vessel (Figure 4D).

In the interest of further characterizing the behavior of SM localization, we grouped and displayed SM subclasses by radyl carbon chain lengths (Figure 5). Each image is a composite of at least three SM components (except for SM with 38 radyl carbons (Figure 5C) that has two). The 38 radyl carbon SM composite image was included to show continuity in the progression of increasing chain lengths in the SM class. Each image shows conservation of some features including the medullary rays, blood vessels, and tubules. For example, 34 radyl carbon SM (Figure 5A) and 42 radyl carbon SM (Figure 5E) are uniquely colocalized to the glomeruli. Based on the localization of monounsaturated SM to the glomeruli (Figure 4C), we presumed and confirmed that a major component was SM(34:1), which was characterized previously as an important mediator for ATP production in glomeruli.[52] It should be noted that for lipids at sufficiently high abundance, other orthogonal analytical approaches such as tandem MS imaging could be used to further validate RKMD annotations and confirm enrichment of certain lipids in a specific tissue region.

The RKMD-based image filtering approach can be applied to any group or subgroup of lipids with increasing specificity down to individual lipid sum compositions, reducing composite images to observe colocalization of very closely related lipids. Of course, lipid sum composition does not describe *sn* position or double-bond position/geometry but is the greatest level of specificity provided by single-stage MS measurement and the RKMD-based method. For example, the 42 radyl carbon SM composite class image (Figure 5E,F) was reduced to the spatial distributions of the three contributing sum compositions, where

SM(42:1), SM(42:2), and SM(42:3) were visualized in an enlarged region of the cortex (Figure 5G–I).

The RKMD-based annotation and image filtering approach provide the framework for an intuitive and data-driven approach for spatial analysis of lipids. High-level class composite images should allow investigators to make broad inferences about their data that inform subsequent interrogations with increasing levels of specificity.

CONCLUSIONS

This work has demonstrated a method for RKMD-based lipid annotation and IMS image filtering. The enhanced specificity and precision of the annotation method were shown through calculation of radyl carbon chain length and dataset curation by exclusion of features with distances from radyl carbon integer values, e, larger than a window defined in this work as 0.001. When applied to peptide, MALDI matrix cluster, and lipid MS features, the specificity and precision were broadly enhanced by radyl carbon e exclusion when compared to conventional exclusion only by RKMD δ or distance from RKMD integer values. A proof-of-concept application to a computationally generated IMS dataset showed the outputs of the method, which were filtered and reconstructed images that use RKMD calculated molecular class, degree of unsaturation, and radyl carbon chain length as criteria.

Finally, we applied the method to MALDI IMS lipidomic data from the human kidney tissue section that spanned the cortex and medulla regions. The filtering method was used to visualize the spatial distribution of subgroups of PC, PE, and SM lipids. Colocalization of saturated PC and PE and monounsaturated SM components was observed throughout the tissue, namely, in glomeruli, medullary rays, and blood vessels. However, the addition of one unsaturation to each molecular class reduced the previously observed correlations between PC/PE and SM. Of particular note was the colocalization of SM to cortical glomeruli. To evaluate the extent of SM localization to glomeruli, we visualized distributions of SM components with varying chain lengths noting unique colocalization of SM with 34 and 42 radyl carbons with glomerular structures. Finally, we reduced the 42 radyl carbon SM composite image to visualize each sum composition component. Building on this work, future studies may utilize this workflow to intuitively analyze spatial distributions of lipid classes within and between samples to enhance the analysis of lipidomics IMS datasets.

Supplementary Material

Refer to Web version on PubMed Central for supplementary material.

ACKNOWLEDGMENTS

REFERENCES

(1). Neumann EK; Migas LG; Allen JL; Caprioli RM; Van de Plas R; Spraggins JM Anal. Chem 2020, 92, 13084–13091. [PubMed: 32668145]

(2). Zhou D; Guo S; Zhang M; Liu Y; Chen T; Li Z Anal. Chim. Acta 2017, 962, 52–59. [PubMed: 28231880]

(3). Dilillo M; Ait-Belkacem R; Esteve C; Pellegrini D; Nicolardi S; Costa M; Vannini E; Graaf ELD; Caleo M; McDonnell LA Sci. Rep 2017, 7, No. 603. [PubMed: 28377615]

(4). Sarabia LD; Boughton BA; Rupasinghe T; Van De Meene AML; Callahan DL; Hill CB; Roessner U Metabolomics 2018, 14, No. 63. [PubMed: 29681790]

(5). Neumann EK; Ellis JF; Triplett AE; Rubakhin SS; Sweedler JV Anal. Chem 2019, 91, 7871–7878. [PubMed: 31122012]

(6). Neumann EK; Comi TJ; Rubakhin SS; Sweedler JV Angew. Chem., Int. Ed 2019, 58, 5910–5914.

(7). Djambazova KV; Klein DR; Migas LG; Neumann EK; Rivera ES; Van de Plas R; Caprioli RM; Spraggins JM Anal. Chem 2020, 92, 13290–13297. [PubMed: 32808523]

(8). Kaya I; Sämfors S; Levin M; Borén J; Fletcher JS J. Am. Soc. Mass Spectrom 2020, 31, 2133–2142. [PubMed: 32897704]

(9). Caprioli RM; Farmer TB; Gile J Anal. Chem 1997, 69, 4751–4760. [PubMed: 9406525]

(10). Do TD; Ellis JF; Neumann EK; Comi TJ; Tillmaand EG; Lenhart AE; Rubakhin SS; Sweedler JV ChemPhysChem 2018, 19, 1180–1191. [PubMed: 29544029]

(11). Taban IM; Altelaar AFM; van der Burgt YEM; McDonnell LA; Heeren RMA; Fuchser J; Baykut GJ Am. Soc. Mass Spectrom 2007, 18, 145–151.

(12). Drake RR; Powers TW; Norris-Caneda K; Mehta AS; Angel PM Curr. Protoc. Protein Sci 2018, 94, No. e68. [PubMed: 30074304]

(13). Gustafsson OJR; Briggs MT; Condina MR; Winderbaum LJ; Pelzing M; McColl SR; Everest-Dass AV; Packer NH; Hoffmann P Anal. Bioanal. Chem 2015, 407, 2127–2139. [PubMed: 25434632]

(14). Powers TW; Neely BA; Shao Y; Tang H; Troyer DA; Mehta AS; Haab BB; Drake RR PLoS One 2014, 9, No. e106255. [PubMed: 25184632]

(15). McDonnell LA; Corthals GL; Willems SM; van Remoortere A; van Zeijl RJ; Deelder AM J. Proteomics 2010, 73, 1921–1944. [PubMed: 20510389]

(16). Goodwin RJA; Pennington SR; Pitt AR Proteomics 2008, 8, 3785–3800. [PubMed: 18712772]

(17). Stoeckli M; Chaurand P; Hallahan DE; Caprioli RM Nat. Med 2001, 7, 493–496. [PubMed: 11283679]

(18). Yèagle PL FASEB J. 1989, 3, 1833–1842. [PubMed: 2469614]

(19). Dennis EA J. Lipid Res 2015, 56, 1245–1247. [PubMed: 26031662]

(20). Walther TC; Farese RV Jr. Annu. Rev. Biochem 2012, 81, 687–714. [PubMed: 22524315]

(21). Spraggins JM; Djambazova KV; Rivera ES; Migas LG; Neumann EK; Fuetterer A; Suetering J; Goedecke N; Ly A; Van de Plas R; Caprioli RM Anal. Chem 2019, 91, 14552–14560. [PubMed: 31593446]

(22). Eriksson C; Masaki N; Yao I; Hayasaka T; Setou M Mass Spectrom. 2013, 2, No. S0022.

(23). Korte AR; Lee YJ J. Mass Spectrom 2014, 49, 737–741. [PubMed: 25044901]

(24). El-Aneed A; Cohen A; Banoub J Appl. Spectrosc. Rev 2009, 44, 210–230.

(25). Bowman AP; Blakney GT; Hendrickson CL; Ellis SR; Heeren RMA; Smith DF Anal. Chem 2020, 92, 3133–3142. [PubMed: 31955581]

(26). Kompauer M; Heiles S; Spengler B Nat. Methods 2017, 14, 90–96. [PubMed: 27842060]

(27). Jeanne Dit Fouque K; Ramirez CE; Lewis RL; Koelmel JP; Garrett TJ; Yost RA; Fernandez-Lima F Anal. Chem 2019, 91, 5021–5027. [PubMed: 30896930]

(28). Murphy RC; Hankin JA; Barkley RM J. Lipid Res 2009, 50, S317–S322. [PubMed: 19050313]

(29). Tang F; Guo C; Ma X; Zhang J; Su Y; Tian R; Shi R; Xia Y; Wang X; Ouyang Z Anal. Chem 2018, 90, 5612–5619. [PubMed: 29624380]

(30). Zhang W; Shang B; Ouyang Z; Xia Y Anal. Chem 2020, 92, 6719–6726. [PubMed: 32271544]

(31). Spiegel MT; Anthony IGM; Brantley MR; Hassell A; Farmer PJ; Solouki T Energy Fuels 2018, 32, 10549–10555.

(32). Kune C; McCann A; Raphaël LR; Arias AA; Tiquet M; Van Kruining D; Martinez PM; Ongena M; Eppe G; Quinton L; Far J; De Pauw E Anal. Chem 2019, 91, 13112–13118. [PubMed: 31509388]

(33). Hughey CA; Hendrickson CL; Rodgers RP; Marshall AG; Qian K Anal. Chem 2001, 73, 4676–4681. [PubMed: 11605846]

(34). Lerno LA; German JB; Lebrilla CB Anal. Chem 2010, 82, 4236–4245. [PubMed: 20426402]

(35). Brewer M; Allen J; Neumann E; Fogo A; Harris R; Gutierrez D; De M; Spraggins J Collection and Post-Surgical Excision of Human Kidney Tissue through the Cooperative Human Tissue Network v1; Vanderbilt University, 2019.

(36). Fahy E; Sud M; Cotter D; Subramaniam S Nucleic Acids Res. 2007, 35, W606–W612. [PubMed: 17584797]

(37). Sud M; Fahy E; Cotter D; Brown A; Dennis EA; Glass CK; Merrill AH Jr.; Murphy RC; Raetz CRH; Russell DW; Subramaniam S Nucleic Acids Res. 2007, 35, D527–D532. [PubMed: 17098933]

(38). Hodson L; Skeaff CM; Fielding BA Prog. Lipid Res 2008, 47, 348–380. [PubMed: 18435934]

(39). Khaw K-T; Friesen MD; Riboli E; Luben R; Wareham N PLoS Med. 2012, 9, No. e1001255. [PubMed: 22802735]

(40). Keller BO; Li LJ Am. Soc. Mass Spectrom 2000, 11, 88–93.

(41). Leopold J; Popkova Y; Engel KM; Schiller J Biomolecules 2018, 8, No. 173. [PubMed: 30551655]

(42). Mamyrin BA Int. J. Mass Spectrom 2001, 206, 251–266.

(43). ezanka T; Sigler K Prog. Lipid Res 2009, 48, 206–238. [PubMed: 19336244]

(44). Zemski Berry KA; Hankin JA; Barkley RM; Spraggins JM; Caprioli RM; Murphy RC Chem. Rev 2011, 111, 6491–6512. [PubMed: 21942646]

(45). Klerk LA; Broersen A; Fletcher IW; Van Liere R; Heeren RM A. Int. J. Mass Spectrom 2007, 260, 222–236.

(46). Alexandrov T BMC Bioinformatics 2012, 13, No. S11.

(47). Buchberger AR; Delaney K; Johnson J; Li L Anal. Chem 2018, 90, 240–265. [PubMed: 29155564]

(48). Verbeeck N; Caprioli RM; Van De Plas R Mass Spectrom. Rev 2020, 39, 245–291. [PubMed: 31602691]

(49). Calvano CD; Monopoli A; Cataldi TRI; Palmisano F Anal. Bioanal. Chem 2018, 410, 4015–4038. [PubMed: 29682685]

(50). Wahl P; Ducasa GM; Fornoni A Am. J. Physiol. Renal Physiol 2016, 310, F433–F445. [PubMed: 26697982]

(51). Harrison-Bernard LM Am. J. Physiol. Renal Physiol 2015, 309, F685–F686. [PubMed: 26155845]

(52). Miyamoto S; Hsu C-C; Hamm G; Darshi M; Diamond-Stanic M; Declèves A-E; Slater L; Pennathur S; Stauber J; Dorrestein PC; Sharma K EBioMedicine 2016, 7, 121–134. [PubMed: 27322466]

(53). Ruh H; Salonikios T; Fuchser J; Schwartz M; Sticht C; Hochheim C; Wirnitzer B; Gretz N; Hopf CJ Lipid Res. 2013, 54, 2785–2794.

(54). Abbas I; Noun M; Touboul D; Sahali D; Brunelle A; Ollero M Int. J. Mol. Sci 2019, 20, No. 1623. [PubMed: 30939806]

(55). Muller L; Kailas A; Jackson SN; Roux A; Barbacci DC; Albert Schultz J; Balaban CD; Woods AS Kidney Int. 2015, 88, 186–192. [PubMed: 25671768]
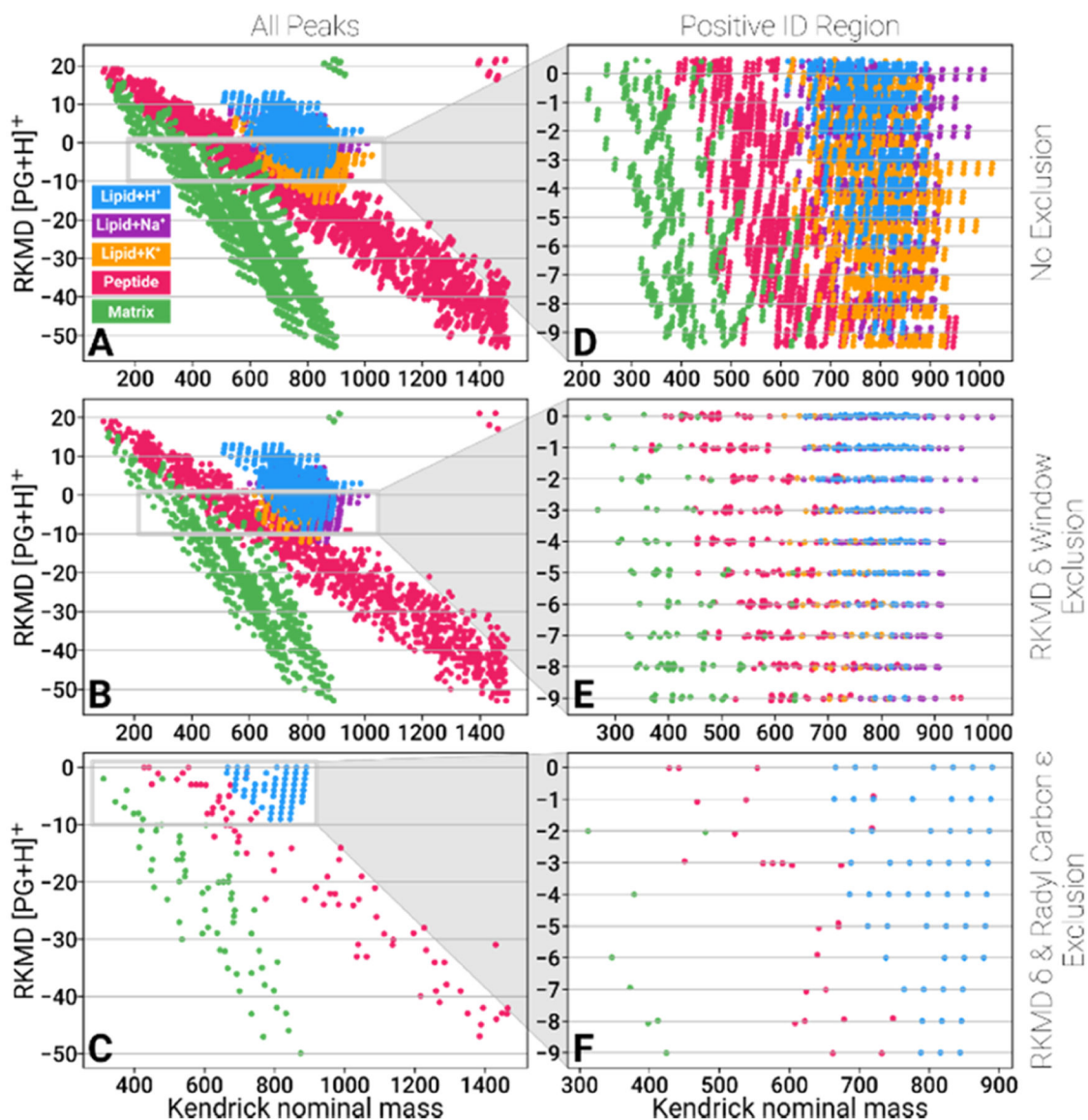
Figure 1.
Computationally generated [PG + H]$^+$ RKMD plots (A–C) with their respective zoomed regions (D–F) demonstrate the utility of using data curation parameters, RKMD δ and radyl carbon ε exclusion windows, to enhance specificity and precision of the RKMD-based annotation method in the presence of protonated lipids (blue, 500 with three isotopes), sodiated lipids (purple, 500 with three isotopes), potassiated lipids (orange, 500 with three isotopes), peptides (pink, 1000 with seven isotopes), and MALDI matrix clusters (green, 1305 with three isotopes). The top row plots (A, D) include all datapoints, plots in the second row (B, E) include datapoints with RKMD δ 0.1, and plots in the third row (C, F) include datapoints with RKMD δ 0.1 and radyl carbon ε 0.001.
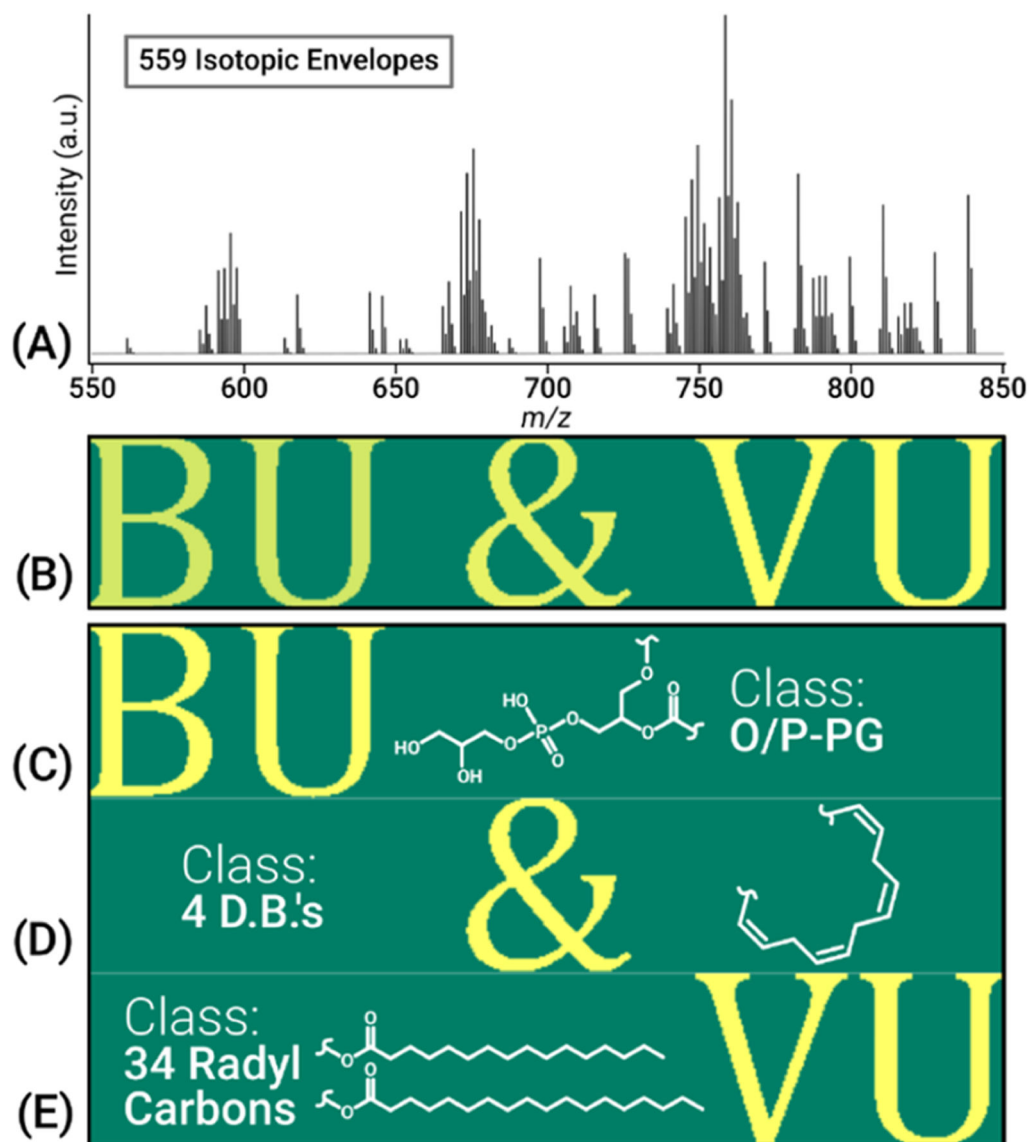
Figure 2.

Computationally generated summed mass spectrum (A) for an MS dataset from 37 044
pixels that included 559 lipids with pseudo-randomized relative abundances was used to
generate the total ion image shown in (B) and a series of RKMD-based filtered mass
spectrometry images (C–E). The total ion current (TIC) image (84 × 441 pixels) in (B)
depicts the summed intensity for each coordinate. The selected class images were filtered
based on molecular class, degrees of unsaturation, and radyl carbon chain length. The
molecular class image (C) was filtered for ether-linked phosphatidylglycerol (O/P-PG)
lipids; the dataset included 86 O/P-PG lipids at the "BU" coordinates. The degree of
unsaturation image (D) was filtered for lipids containing 4 unsaturations; this dataset
included 216 lipids containing PC, PA, PG, or DG headgroups and all contained four double
bonds at the "&" coordinates. The radyl carbon chain length image (E) was filtered for lipids

with 34 radyl carbons; the dataset included 257 lipids with 34 radyl carbons from the same four molecular classes.
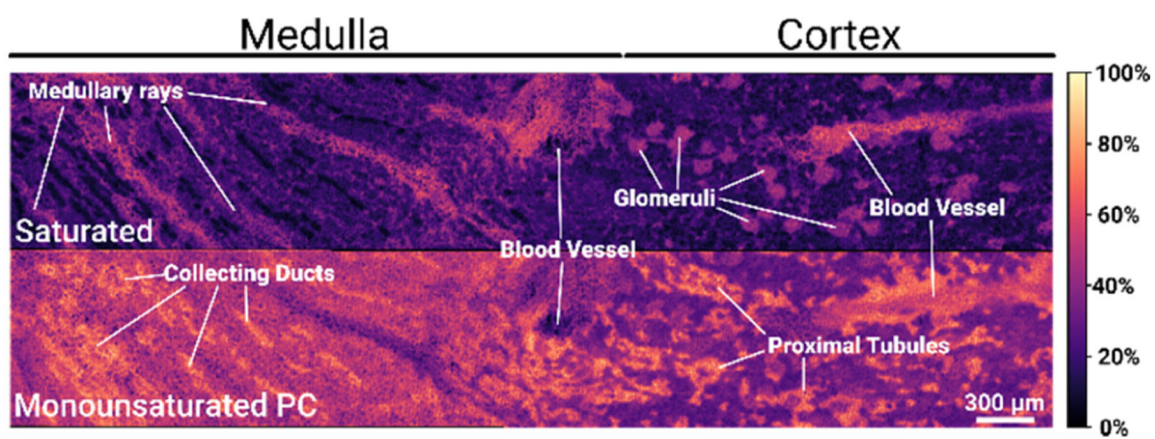
Figure 3.
Labeled renal tissue structures spanning parts of the medulla and cortex region in class composite images depicting saturated (top) and monounsaturated PC (bottom).
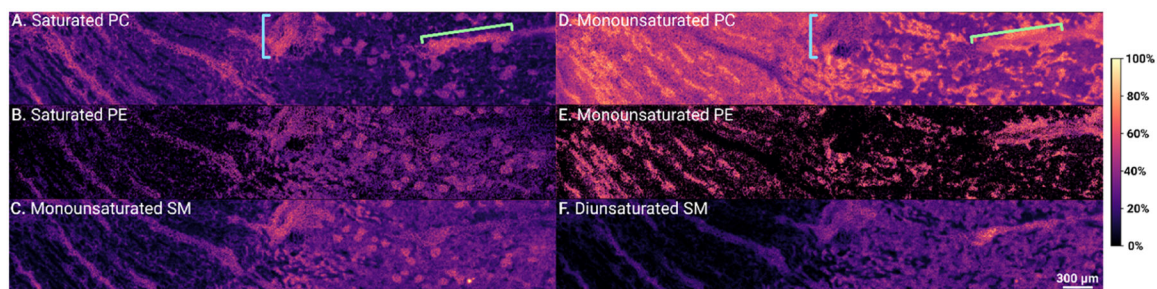
Figure 4.
RKMD-based filtering applied to a MALDI IMS dataset from human kidney sections with the medulla and cortex visible in all images: (A) saturated PC, (B) saturated PE, (C) monounsaturated SM, (D) monounsaturated PC, (E) monounsaturated PE, and (F) diunsaturated SM. Images generated by RKMD-based filtering can be used to rapidly determine lipid trends among functional regions.
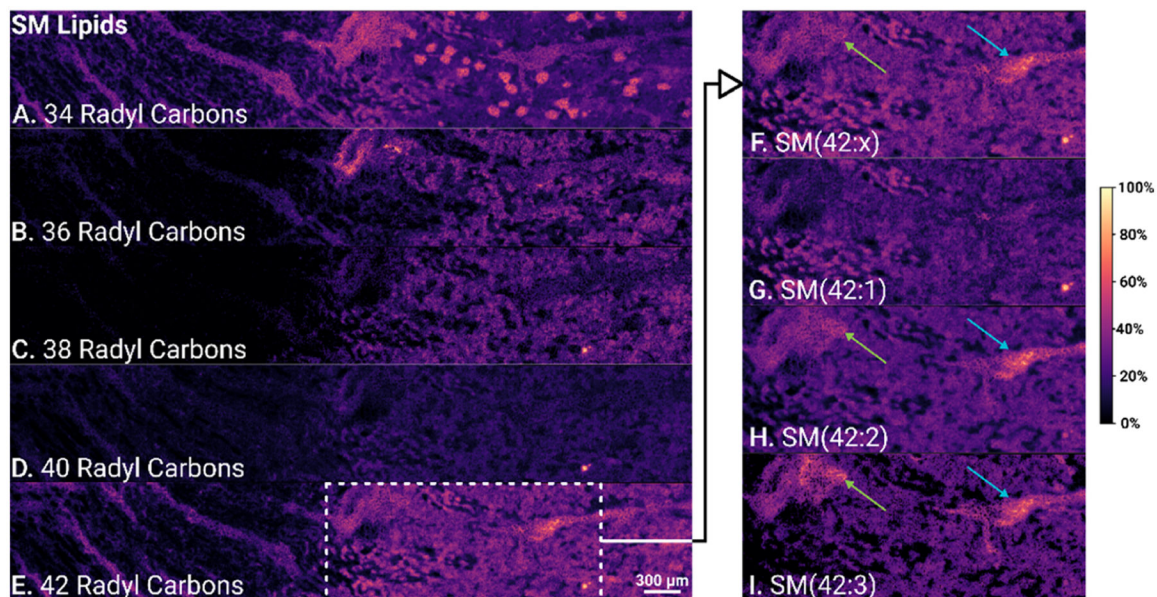
Figure 5.
RKMD-based filtering applied to a MALDI IMS dataset from human kidney section SM lipids with 34, 36, 38, 40, and 42 radyl carbons in (A–E) followed by an enlarged region for SM with 42 radyl carbons (F) with further classifications for 1 (G), 2 (H), and 3 (I) unsaturations. Green and blue arrows indicate blood vessels represented in the 42 radyl carbon SM composite (F) that are colocalized to SM(42:2) (H) and SM(42:3) (I) and absent in SM(42:1) (G). Reducing class composite images enables localization of discrete sum compositions and attribution of observed morphological features to more specific groups of lipids.